Research
Robotics—Article

A Novel Tele-Operated Flexible Robot Targeted for Minimally Invasive Robotic Surgery

Zheng Li[1,3,4*], Jan Feiling[2], Hongliang Ren[1], Haoyong Yu[1]

ABSTRACT In this paper, a novel flexible robot system with a constrained tendon-driven serpentine manipulator (CTSM) is presented. The CTSM gives the robot a larger workspace, more dexterous manipulation, and controllable stiffness compared with the *da Vinci* surgical robot and traditional flexible robots. The robot is tele-operated using the Novint Falcon haptic device. Two control modes are implemented, direct mapping and incremental mode. In each mode, the robot can be manipulated using either the highest stiffness scheme or the minimal movement scheme. The advantages of the CTSM are shown by simulation and experimental results.

1 Introduction

Surgical robots with flexible manipulators (FMs) have the potential to revolutionize minimally invasive robotic surgery (MIRS) [1]. Their advantages over traditional rigid-arm surgical robots, represented by the *da Vinci* surgical robot system, include: ① safer surgical intervention; ② the ability to explore a much wider range inside the body; and ③ the ability to manipulate inside the body without pivoting around the trocar. These advantages have driven Intuitive Surgical to develop the latest *da Vinci* Sp surgical system, which is equipped with FMs [2].

Current FMs mainly fall into two categories: the tendon-driven manipulator (TM), whose flexible backbone can be serpentine (TSM) [3, 4] or continuum (TCM) [5, 6]; and the concentric tube manipulator (CTM) [7, 8]. In traditional TMs, the flexible backbone is bent by the tendons (sometimes called cables or wires [9]). The curvature of the backbone is controllable, while the length of the bending section is fixed. In the CTMs, several pre-curved tubes are nested concentrically. By inserting and rotating the inner tubes with regard to the outer tubes, the overall shape of the flexible backbone is controlled. The curvature of the distal bending section of the CTMs is fixed. The limited control of the bending section in existing mechanisms constrains the workspace and dexterity of the robot. Although this could be alleviated by introducing more bending sections, the tradeoff is that the system becomes much more complicated. The HARP robot [10] uses two concentric TMs, which can bend to any desired shapes. However, the movement of the HARP is very slow. Another common drawback of FMs is the limited payload ability, due to the low stiffness of the flexible backbone. The limitations of existing FMs raise the demand for a new FM design, in which both the curvature and length of the bending section are controllable, and in which the backbone stiffness is tunable.

In this paper, we present a novel TSM design, which employs a constraint tube to expand the workspace and enhance dexterity [11, 12]. It is named the constrained tendon-driven serpentine manipulator (CTSM). The stiffness of the CTSM can be tuned in two ways: by controlling the tendon tensions simultaneously as in traditional TSMs [13], and by controlling the length of the bending section. A robot utilizing the CTSM was developed. It is tele-operated using the Novint Falcon haptic device [14]. Two motion-control modes are implemented: direct mapping and incremental mode. The results given in this paper are modified from those in our ongoing conference paper [15]. The rest of the paper is organized as follows: Section 2 presents the flexible robot system design and tele-operation scheme; Section 3 gives the kinematic modeling; Section 4 gives the optimal control of the robot; Section 5 shows the robot prototype and experimental results; and Section 6 concludes the paper.

2 The flexible robot system

The flexible robot is composed of the robot structure, the micro controller, and the input device (the Novint Falcon haptic device).

---

[1] Department of Biomedical Engineering, National University of Singapore, Singapore 119077, Singapore; [2] Faculty of Design, Production Engineering, and Automotive Engineering, University of Stuttgart, 70569 Stuttgart, Germany; [3] Institute of Digestive Disease, the Chinese University of Hong Kong, Hong Kong, China; [4] Chow Yuk Ho Technology Centre for Innovative Medicine, the Chinese University of Hong Kong, Hong Kong, China
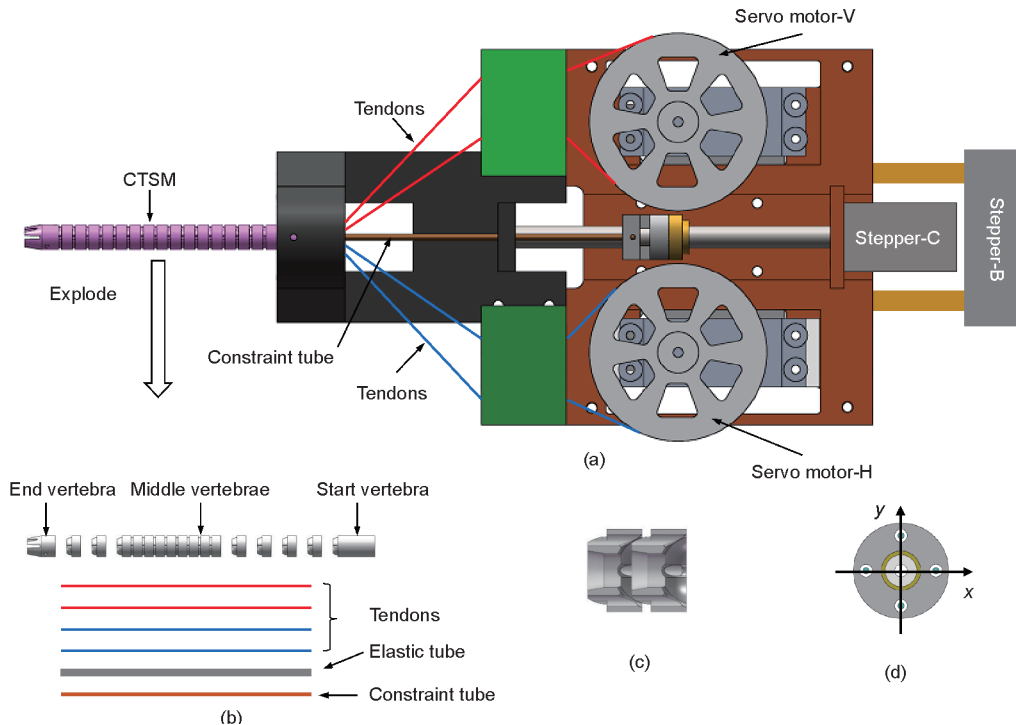* Correspondence author. E-mail: lizheng@cuhk.edu.hk

Figure 1. Mechanical design of the flexible surgical robot. (a) Constrained tendon-driven serpentine manipulator (CTSM); (b) explosion view of the CTSM; (c) cross-section view of the joint; (d) tendon configuration.

2.1 Mechanical design of the flexible robot

The design of the robot structure is shown in Figure 1. It comprises two parts: the CTSM and the driving module. The CTSM design is developed based on our previous TSM designs [3, 4]. It contains a chain of short vertebrae, with two adjacent vertebrae forming a joint, a set of tendons, an elastic tube, and a constraint tube. The elastic tube regulates the rotation of the joints, which is controlled by the tendons. In the CTSM, the number of joints can be modified as desired without increasing the number of tendons. The constraint tube is concentric with the elastic tube. It is rigid and can translate along the flexible backbone, which is composed of the vertebrae and the elastic tube. Since the constraint tube is rigid, in the flexible backbone the section overlapping with the constraint tube cannot be rotated. The rest section (bending section) can be bent by the tendons. Therefore, by controlling the position of the constraint tube, the length of the bending section is controlled. The driving module is composed of two servo motors and two stepper motors. As illustrated in Figure 1, the two servo motors control the bending of the CTSM through tendons: "Servo motor-V" controls the up/down bending and "servo motor-H" controls the left/right bending. The constraint tube is controlled by the "stepper-C" and the base of the robot is controlled by the "stepper-B".

The bending motion of the CTSM is illustrated in Figure 2. In the figure, the constraint tube advances from the base toward the distal end of the flexible backbone as shown by (a)–(c). The highlighted blocks represent the constrained vertebrae. The trajectory of the distal end during backbone bending is controlled by the tendons and the constraint tube. It is noted that, when the constraint tube is immobilized, the bending motion of the CTSM is the same as a TSM.
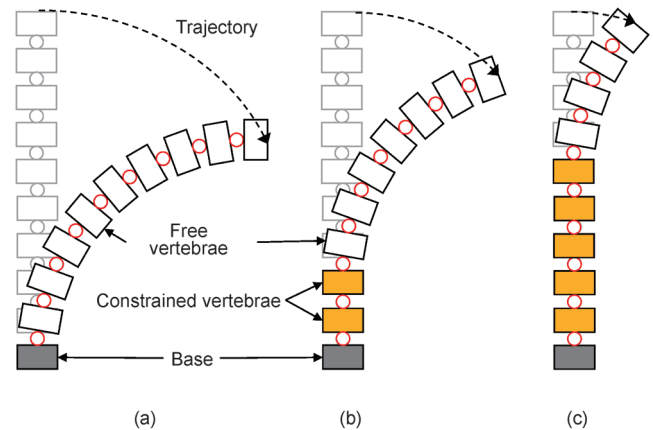

Figure 2. Bending motion illustration of the CTSM.

2.2 Tele-operation scheme

The robot is controlled using the Novint Falcon [14], which is a low-cost haptic device that can provide the spatial position of the knob. The tele-operation scheme is shown in Figure 3. The Novint Falcon serves as the master controller. The knob position of the Novint Falcon is sent to Matlab$^{©}$, and the program solves the control inputs to the motors. The micro controller (Arduino Mega 2560) converts the control inputs to PWM signals, which control the motion of the motors.

Two control modes can be implemented. One is the direct mapping mode, in which the workspace of the Novint Falcon is mapped to the workspace of the flexible robot by some scaling factor. The end effector of the CTSM follows the motion of the knob continuously. In the second mode, the robot is moved incrementally by the knob with the assistance of the buttons on the knob. The details are described in the following section.
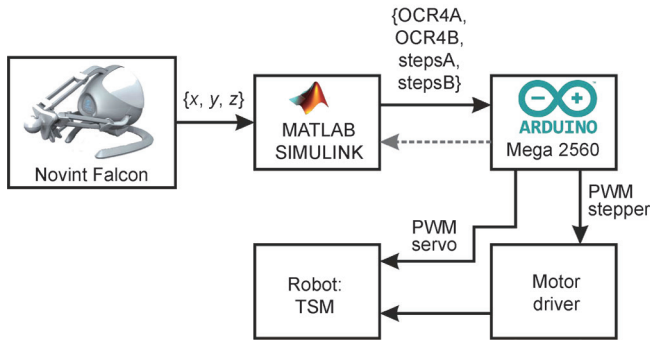
Figure 3. The scheme of the tele-operation.

3 Kinematic modeling

3.1 Kinematics model

The kinematics model is composed of the four mappings, as shown in Figure 4. The "device-actuator space mapping" (f_4) is fundamental in robot control. It can be derived from the other three mappings: the "actuator-joint space mapping" (f_1), the "joint-task space mapping" (f_2) and the "task-device space mapping" (f_3). The following gives a summary; this derivation is similar to that in our previous work [3, 4, 11]. The coordinate frame setting and nomenclature are given in Figure 5.
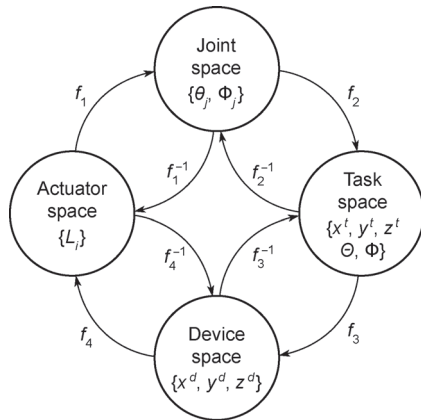

Figure 4. Kinematics mappings.

(1) Actuator-joint space mapping (f_1):

$$\begin{cases} L_1 = L_0 + 2N_f\left[b\cdot\sin\left(\frac{\theta}{2}\right) - h_0\cdot\sin^2\left(\frac{\theta}{4}\right)\right] \\ L_2 = L_0 + 2N_f\left[a\cdot\sin\left(\frac{\theta}{2}\right) - h_0\cdot\sin^2\left(\frac{\theta}{4}\right)\right] \\ L_3 = L_0 - 2N_f\left[b\cdot\sin\left(\frac{\theta}{2}\right) + h_0\cdot\sin^2\left(\frac{\theta}{4}\right)\right] \\ L_4 = L_0 - 2N_f\left[a\cdot\sin\left(\frac{\theta}{2}\right) + h_0\cdot\sin^2\left(\frac{\theta}{4}\right)\right] \\ L_t = (N - N_f)l = N_c\cdot l \end{cases} \quad (1)$$

in which $a = \frac{d}{2}\sin(\Phi)$ and $b = \frac{d}{2}\cos(\Phi)$ are the distances of the tendons to the bending neutral plane as in Ref. [3]; L_0 is
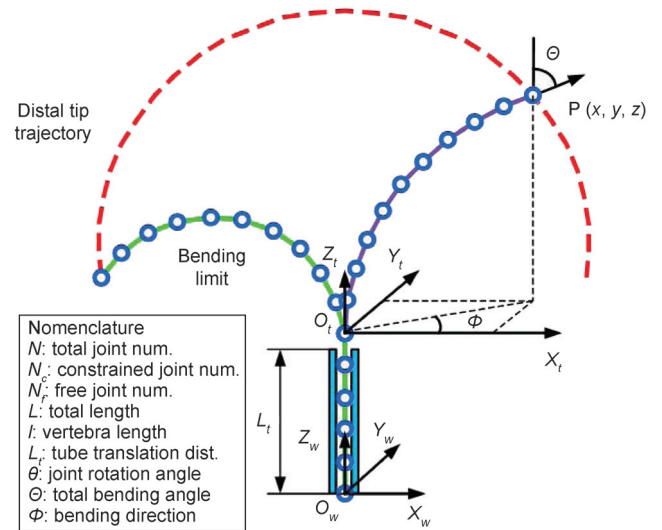

Figure 5. Coordinate setting and nomenclature.

the length of the tendons and h_0 is the joint gap distance, both at resting position; and d is the distance between the tendons in a pair.

(2) Joint-task space mapping (f_2): The distal end position $\mathbf{x}^t = \{x^t, y^t, z^t\}$ of the CTSM in the task space is:

$$\begin{cases} x^t = R\cdot\sin\left[(N_f+1)\frac{\theta}{2}\right]\cos(\Phi) \\ y^t = R\cdot\sin\left[(N_f+1)\frac{\theta}{2}\right]\sin(\Phi) \\ z^t = R\cdot\cos\left[(N_f+1)\frac{\theta}{2}\right] + z_b + N_c l \end{cases} \quad (2)$$

in which $R = l\dfrac{\sin\left(N_f\theta/2\right)}{\sin(\theta/2)}$, and z_b is the base movement along the Z_w axis.

(3) Task-device space mapping (f_3): The task-device space mapping is directly related to the CTSM motion control in the tele-operation. The inverse mapping in the two motion modes is given. In the direct mapping mode, f_3 is straightforward.

$$\mathbf{x}^t = \boldsymbol{k}\cdot\mathbf{x}^d, \quad \exists \boldsymbol{k} \in \mathbf{R}^3 : 0 < k_{1,2,3} \leqslant 1 \quad (3)$$

where $\mathbf{x}^d$ is the desired position and the vector $\boldsymbol{k}$ includes the scaling factors.

In the incremental mode, the CTSM end effector is not controlled by the position of the knob, but by the stroke in each movement cycle when the button is pressed. The inverse mapping (f_3^{-1}) is below:

$$\mathbf{x}_i^t = \mathbf{x}_{i-1}^t + \boldsymbol{k}\cdot\left[\mathbf{x}_i^d - \mathbf{x}_{i-1}^d\right] \quad (4)$$

3.2 Simulation results

A comparison between the traditional TSM and the CTSM was performed based on simulation. In the simulation, both the TSM and the CTSM contain 25 vertebrae and the total length is 100 mm. The maximum joint rotation is 7.2°. Figure 6 gives the results of workspace comparison. By introducing the constraint tube, the workspace of the manipulator is much expanded.
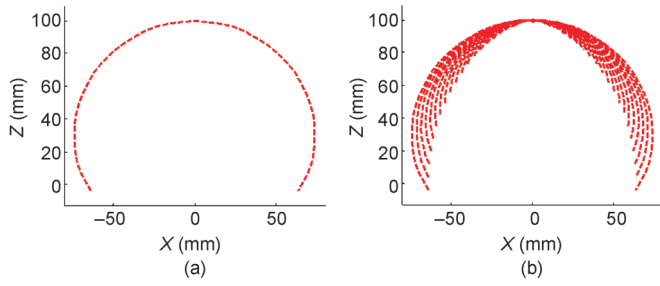
Figure 6. Workspace comparison. (a) Traditional TSM; (b) CTSM.

In the dexterity comparison, the manipulator accesses the target position P_d (65, 0, 50). Figure 7 gives the results. The TSM can access the target with only one configuration, while the CTSM can access P_d with five configurations. This result shows that at this position, the CTSM is five times more dexterous than the TSM. It should be noted that the dexterity is related to the position of the target. On average, the dexterity of the CTSM is 4.7 times that of the TSM.
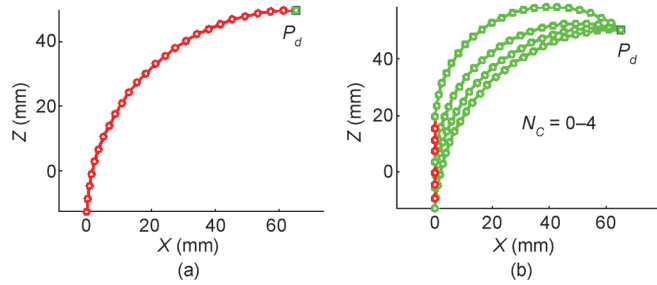

Figure 7. Dexterity comparison. (a) Traditional TSM; (b) CTSM.

4 Optimal control scheme

As seen in the previous section, the CTSM has a plurality of configurations for accessing the target. This gives the opportunity to control the robot with an optimal strategy based on needs. In this section, two optimal strategies are proposed.

4.1 Highest stiffness

As mentioned in the introduction, the stiffness of the CTSM can be controlled in two ways. In this section, we focus on the method of controlling the backbone-bending configuration.

The CTSM structure is similar to a cantilever beam, the stiffness of which is proportional to the cube of the backbone length. Hence, in the highest stiffness control mode we choose the shortest length of the bending section. If the set of the solution to the target P_d is $\{N_f, \theta, \Phi\}$, the optimal solution is:

$$N_c^*(x, y) = \max\{\mathbf{N}_c(x, y)\} \tag{5}$$

where $\mathbf{N}_c$ is the set of possible solutions in the inverse kinematics.

It is noted that the base of the CTSM is translational, and the CTSM can bend in all directions with equal effort. Therefore the number of solutions depends on the lateral displacement $\sqrt{x^2 + y^2}$ only. This can be solved in advance. Noting that $N = N_c + N_f$ from the previous model, the lateral displace-

ment is:

$$\sqrt{x^2 + y^2} = R \cdot \sin\left[(N - N_c + 1)\frac{\theta}{2}\right] \tag{6}$$

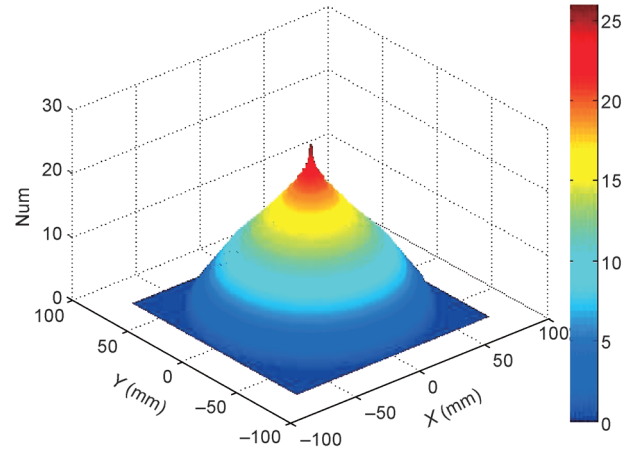Figure 8 gives the number of solutions to Eq. (6) with the same parameters as in the previous simulation.

Figure 8. Number of solutions for $N = 25$ and $l = 4$.

4.2 Minimal movements

For minimal movements, a penalty function to optimize N_c is employed. It includes the difference of N_c and z_0 of each time step $(i, i-1)$, a vector $\mathbf{r}$ that includes the penalty factors r_1 and r_2, and two weight factors, α and β. The factor α is the scaling for the steps of the base motor (stepper-B) and the factor β is a weight factor to reduce the movements of the constraint motor (stepper-C). The constraints for the boundary minimum problem are:

$$N_c^*(x, y) \leqslant N_c^{\max}(x, y) \text{ and } z_0^* \leqslant z_0^{\max} \tag{7}$$

With the constraint (7) and the weight factors, the following penalty function is developed:

$$
\begin{aligned}
P(N_c^i, \mathbf{r}) = &\| z_b^i(N_c^i, \theta(x, y, N_c^i)) - z_b^{i-1} \| \alpha \\
&+ \| N_c^i - N_c^{i-1} \| \beta \\
&+ r_1 \min\{0, N_c^{\max,i}(x, y) - N_c^i\}^2 \\
&+ r_2 \min\{0, z_b^{\max} - z_b^i\}^2
\end{aligned}
\tag{8}
$$

Using the Nelder-Mead Simplex method [16], we find the minimum of Eq. (8) and get:

$$N_c^* = \min\{P(N_c^i, \mathbf{r})\} \tag{9}$$

5 Prototype and experimental results

A prototype was developed, as shown in Figure 9. The outer diameter of the vertebrae is 7.5 mm. In the middle of the vertebrae there is a 3 mm hole for the elastic tube and constraint tube. The length of each vertebra is 3.2 mm. Two successive vertebrae form a joint and each joint can rotate up to 7.25°. The number of vertebrae can be changed as desired. In the following tests, the CTSM has 20 vertebrae. The CTSM is controlled by four motors: Two servo motors control the bending, one stepping motor controls the movement of the constraint

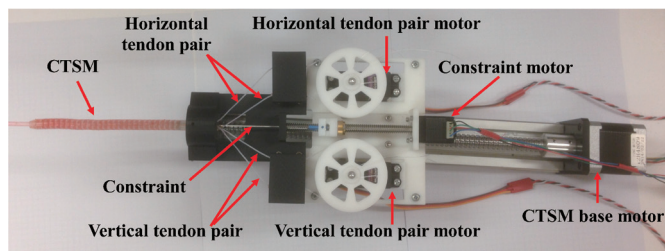tube, and another stepping motor controls the movement of the CTSM base.

Figure 9. Prototype of the flexible robot.

Three experiments were carried out to demonstrate the performance of the CTSM. The first involves target approaching in a confined environment, and the second is a weight-lifting test. In both tests, the robot is controlled in four modes: ① direct mapping with highest stiffness; ② direct mapping with minimal movements [$\alpha = 1$, $\beta = 25$]; ③ direct mapping with minimal movements [$\alpha = 10$, $\beta = 1$]; and ④ incremental mode with highest stiffness. In the third experiment, the CTSM is controlled to explore the nasal cavity, mimicking transnasal surgery.

Experiment 1—Target approaching in a confined environment: The CTSM is controlled to tap three targets in a confined environment starting from the resting position, as shown in Figure 10(a). The opening of the plastic bottle mimics the trocar, and the targets mimic the places of interest in the MIRS. Figure 11 shows the trajectory of the CTSM end effector in the four control modes. In the figure, the three cross markers represent the targets and the dots denote the positions of the distal end of the CTSM at different time instances (corresponding to the colorbar at the bottom). The time between two consecutive points is one second. From the results, the CTSM successfully approaches the vicinity of the three targets in all four modes. The time consumed in mode ③ is the shortest (29 s) and in mode ① is the longest (47 s). Based on the tapping accuracy, modes ② and ④ are much better than modes ① and ③. In MIRS, accuracy is more important than speed. Therefore, the incremental mode is better suited in MIRS than the direct mapping mode. To improve the positioning accuracy in the direct mapping mode, the minimal movement scheme can be adopted.

Experiment 2—Weight-lifting test: The CTSM is controlled to a target position and then a 10 g weight is placed on the tip of the CTSM, as shown in Figure 10(b). After 15 s of random
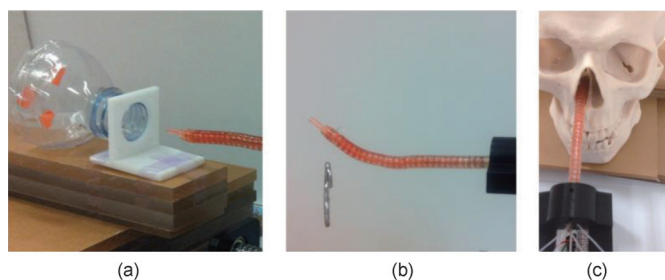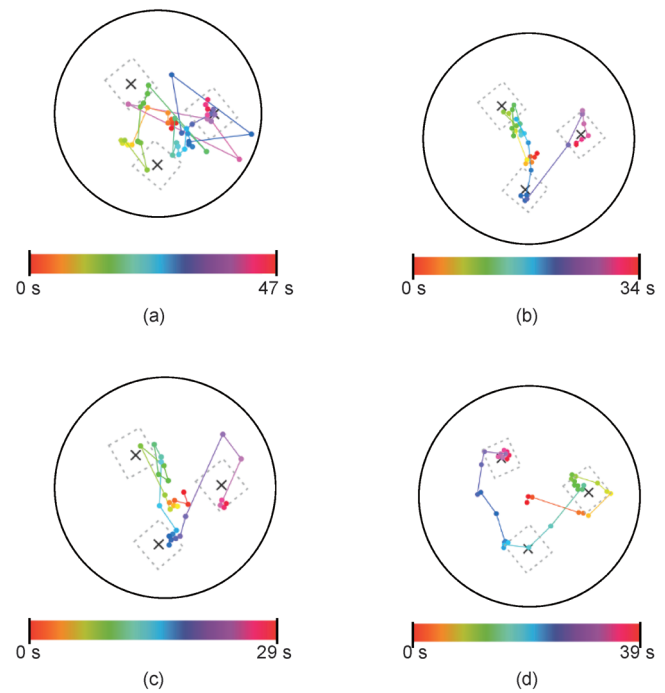

Figure 11. Distal end trajectories in the four control modes in experiment 1. (a) Direct mapping with highest stiffness; (b) direct mapping with minimal movements [$\alpha = 1$; $\beta = 25$]; (c) direct mapping with minimal movements [$\alpha = 10$; $\beta = 1$]; (d) incremental mode with highest stiffness.

movements, the CTSM is controlled to access the target again. The deformation of the backbone is compared in Figure 12. In the figure, the green-colored area is the deformed backbone, and the light blue area is the initial backbone shape. In mode ①, the CTSM gets to the target with negligible error. In mode ④, the deformation is slightly larger but remains small. In mode ② and mode ③, the backbone deformation is much larger than in the highest stiffness modes. In particular, mode ② has the largest deformation, as it is in fact the minimal stiffness mode.

Experiment 3—Nasal cavity exploring: The CTSM is controlled to "explore" the nasal cavity through the nostril of a skull phantom, as shown in Figure 10(c). Both the direct mapping mode and the incremental mode were tested. Experience shows that in the direct mapping mode, the CTSM can move close to the nostril quickly, but cannot easily point to the nostril and enter it due to hand tremor. On the other hand, in the incremental mode, the CTSM moves toward the nostril

Figure 10. Experiment testing. (a) Target approaching in a confined environment; (b) weight-lifting test; (c) nasal cavity exploring test.

Figure 12. Deformation of the distal after 15 s moving with light blue color at *t* = 0 s and green color at *t* = 15 s. (a) Direct mapping with highest stiffness; (b) direct mapping with minimal movements [$\alpha = 1$; $\beta = 25$]; (c) direct mapping with minimal movements [$\alpha = 10$; $\beta = 1$]; (d) incremental mode with highest stiffness.

slowly but can enter the nostril much more easily and can be better maneuvered inside the nasal cavity. Therefore, a combination of the two modes is favorable. Two snapshots during the test are shown in Figure 13. During the exploration, the CTSM does not require pivoting around the entry point as does the *da Vinci* robot. As the nostril is narrow and deep, reduced pivoting can reduce the trauma to the nostril.
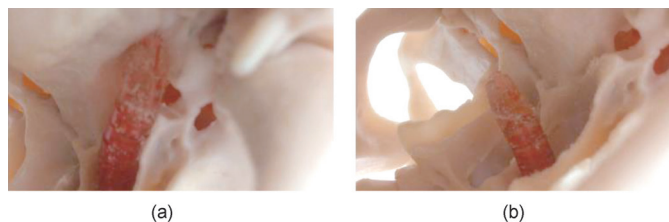

(a)   (b)

Figure 13. Snapshots in the nasal cavity exploring test.

6 Conclusions

This paper presents a novel tele-operated flexible robot with a constrained tendon-driven serpentine manipulator (CTSM). In the CTSM, both the length and curvature of the bending section are controllable, which brings multiple benefits including expanded workspace, enhanced dexterity, and controllable stiffness. Two tele-operation modes are implemented and evaluated. The direct mapping mode enables fast motion, while the incremental mode entails better accuracy. In the future, functional tools, such as a micro camera, forceps, needles, and so on will be added to the robot, resulting in a flexible robot for MIRS.

Acknowledgements

Compliance with ethics guidelines

Zheng Li, Jan Feiling, Hongliang Ren, and Haoyong Yu declare that they have no conflict of interest or financial conflicts to disclose.

References

1. H. Ren, et al. Computer-assisted transoral surgery with flexible robotics and navigation technologies: A review of recent progress and research challenges. *Crit. Rev. Biomed. Eng.*, 2013, 41(4–5): 365–391

2. Medgadget LLC. Intuitive's new da Vinci Sp single port minimally invasive robotic system (VIDEO). 2014-04-23. http://www.medgadget.com/2014/04/intuitives-new-da-vinci-sp-single-port-minimally-invasive-robotic-system-video.html

3. Z. Li, R. Du. Design and analysis of a bio-inspired wire-driven multi-section flexible robot. *Int. J. Adv. Robot. Syst.*, 2013, 10: 1–9

4. Z. Li, R. Du, M. C. Lei, S. M. Yuan. Design and analysis of a biomimetic wire-driven robot arm. In: *Proceedings of the ASME 2011 International Mechanical Engineering Congress and Exposition*, 2011: 191–198

5. K. Xu, J. Zhao, M. Fu. Development of the SJTU unfoldable robotic system (SURS) for single port laparoscopy. *IEEE/ASME Trans. Mechatron.*, 2014(99): 1–13

6. N. Simaan, R. Taylor, P. Flint. A dexterous system for laryngeal surgery. In: *Proceedings of IEEE International Conference on Robotics and Automation*, vol. 1. IEEE, 2004: 351–357

7. J. Burgner, et al. A telerobotic system for transnasal surgery. *IEEE/ASME Trans. Mechatron.*, 2013, 19(3): 996–1006

8. P. E. Dupont, J. Lock, B. Itkowitz, E. Butler. Design and control of concentric-tube robots. *IEEE Trans. Robot.*, 2010, 26(2): 209–225

9. G. Lum, S. Mustafa, H. Lim, W. Lim, G. Yang, S. Yeo. Design and motion control of a cable-driven dexterous robotic arm. In: *Proceedings of IEEE Conference on Sustainable Utilization and Development in Engineering and Technology (STUDENT)*. IEEE, 2010: 106–111

10. A. Degani, H. Choset, A. Wolf, M. A. Zenati. Highly articulated robotic probe for minimally invasive surgery. In: *Proceedings of IEEE International Conference on Robotics and Automation*. IEEE, 2006: 4167–4172

11. Z. Li, R. Du. Expanding workspace of underactuated flexible manipulator by actively deploying constrains. In: *Proceedings of IEEE International Conference on Robotics and Automation*. IEEE, 2014: 2901–2906

12. Z. Li, H. Yu, H. Ren. A novel underactuated wire-driven flexible robotic arm with controllable bending section length (abstract). In: *ICRA 2014 Workshop on Advances in Flexible Robots for Surgical Interventions*, 2014: 11

13. Z. Li, R. Du, H. Yu, H. Ren. Statics modeling of an underactuated wire-driven flexible robotic arm. In: *Proceedings of IEEE RAS & EMBS International Conference on Biomedical Robotics and Biomechatronics*. IEEE, 2014: 326–331

14. Novint Falcon haptic device. [2014-03-11]. http://www.novint.com/index.php/novintfalcon

15. J. Feiling, Z. Li, H. Ren, H. Yu. The constrained tendon-driven serpentine manipulator and its optimal control using novint falcon. In: *The 28th Canadian Conference on Electrical and Computer Engineering*, 2015 (in press)

16. K. Klein, J. Neira. Nelder-Mead simplex optimization routine for large-scale problems: A distributed memory implementation. *Comput. Econ.*, 2014, 43(4): 447–461